

## ARTICLE OPEN



# Cholesterol biosynthetic pathway induces cellular senescence through ER $\alpha$

Dorian V. Ziegler<sup>1</sup>, Joanna Czarnecka-Herok<sup>1,2</sup>, Mathieu Vernier<sup>1,2,3</sup>, Charlotte Scholtes<sup>3</sup>, Clara Camprubi<sup>1</sup>, Anda Huna<sup>1,2</sup>, Amélie Massemin<sup>1,2</sup>, Audrey Griveau<sup>1</sup>, Christelle Machon<sup>4</sup>, Jérôme Guitton<sup>4</sup>, Jennifer Rieusset<sup>5</sup>, Arnaud M. Vigneron<sup>1</sup>, Vincent Giguère<sup>3,6</sup>, Nadine Martin<sup>1,2,7</sup>✉ and David Bernard<sup>1,2,7</sup>✉

Cellular senescence is a cell program induced by various stresses that leads to a stable proliferation arrest and to a senescence-associated secretory phenotype. Accumulation of senescent cells during age-related diseases participates in these pathologies and regulates healthy lifespan. Recent evidences point out a global dysregulated intracellular metabolism associated to senescence phenotype. Nonetheless, the functional contribution of metabolic homeostasis in regulating senescence is barely understood. In this work, we describe how the mevalonate pathway, an anabolic pathway leading to the endogenous biosynthesis of poly-isoprenoids, such as cholesterol, acts as a positive regulator of cellular senescence in normal human cells. Mechanistically, this mevalonate pathway-induced senescence is partly mediated by the downstream cholesterol biosynthetic pathway. This pathway promotes the transcriptional activity of ER $\alpha$  that could lead to dysfunctional mitochondria, ROS production, DNA damage and a p53-dependent senescence. Supporting the relevance of these observations, increase of senescence in liver due to a high-fat diet regimen is abrogated in ER $\alpha$  knockout mouse. Overall, this work unravels the role of cholesterol biosynthesis or level in the induction of an ER $\alpha$ -dependent mitochondrial program leading to cellular senescence and related pathological alterations.

*npj Aging* (2024)10:5; <https://doi.org/10.1038/s41514-023-00128-y>

## INTRODUCTION

Cellular senescence is a program promoted by a myriad of stresses such as telomeres shortening, oncogenic stress-induced hyper-replication and oxidative stress-mediated damages<sup>1</sup>. This program is characterized by a permanent cell cycle arrest and a senescence-associated secretory phenotype (SASP)<sup>1</sup>, both implicated in the pathophysiological effects of senescent cells<sup>2,3</sup>. Senescence-associated pathophysiological contexts include development, tissue regeneration, cancer and aging<sup>2,3</sup>. Although timely regulated senescence exerts beneficial effects, the accumulation of senescent cells throughout life and upon exposure to chronic stresses exerts detrimental effects by promoting aging and its associated diseases<sup>4–9</sup>. Mechanistically, while downstream factors and effectors, such as p53, p21<sup>CIP1</sup> and p16<sup>INK4A</sup> or NF- $\kappa$ B and C/EBP $\beta$ , respectively blocking cell cycle progression or promoting SASP, were extensively studied<sup>1–3</sup>, upstream molecular and subcellular mechanisms controlling these factors are less understood.

Senescent cells harbour metabolic changes related to both catabolism and anabolism<sup>1,10–15</sup>, to the point that some metabolic specificities of senescent cells are used to target or detect them<sup>11,16,17</sup>. Indeed, senescent cells display metabolic rearrangements as evidenced for instance by an altered glycolytic state and glucose utilization<sup>11,12,18</sup>, a deregulated mitochondrial metabolism, an AMPK activation and an altered NAD<sup>+</sup> metabolism<sup>10,19–22</sup>. Lipid metabolism is also modified in senescent cells<sup>15,23–30</sup>. For instance, senescent hepatocytes<sup>26,27</sup>, fibroblasts<sup>31</sup>, and T-cells<sup>32</sup> display an accumulation of lipid droplets (LD), this later accounting mostly for an increase of free fatty acids<sup>23</sup> and free

cholesterol<sup>25,28</sup>, subsequently esterified and incorporated in LD via triglycerides (TG) or cholesteryl esters. The mevalonate (MVA) pathway is part of lipid anabolism and involved in the endogenous biosynthesis of poly-isoprenoids, such as prenyl groups, ubiquinone, cholesterol or dolichol<sup>33</sup>. MVA pathway is thus crucial for many cellular processes including protein-protein interactions, mitochondrial respiration, membranes fluidity or glycosylation<sup>33</sup>. Some studies using pharmacological tools, such as statins or bisphosphonates, have previously suggested an involvement of this pathway in regulating senescence, still with some contradictory effects reported<sup>34,35</sup>. Furthermore, how endogenous cholesterol biosynthesis mechanistically regulate cellular senescence remains so far elusive. Interestingly, in a functional genetic screen of a constitutively active kinase library that we previously reported<sup>36</sup>, two kinases of the MVA pathway, mevalonate kinase (MVK) and phosphomevalonate kinase (PMVK), were identified as able to induce premature senescence when ectopically expressed. Still the mechanisms of action of these enzymes in this context and the relevance of these observations during senescence in vivo remained unknown.

In this study, we assessed through the use of genetic tools whether and how the MVA pathway and the downstream biomolecules regulate cellular senescence. Unexpectedly, this work led to the identification of a new mechanism regulating senescence: a cholesterol-dependent ER $\alpha$  transcriptional program leading to mitochondrial dysregulation and senescence-associated liver alterations.

<sup>1</sup>Centre de Recherche en Cancérologie de Lyon, Inserm U1052, CNRS UMR 5286, Centre Léon Bérard, Université de Lyon, Lyon, France. <sup>2</sup>Equipe Labellisée la Ligue Contre le Cancer, Lyon, France. <sup>3</sup>Goodman Cancer Research Centre, McGill University, Quebec, Montreal, Canada. <sup>4</sup>Biochemistry and Pharmacology-Toxicology Laboratory, Lyon-Sud Hospital, Hospices Civils de Lyon, F-69495 Pierre Bénite, France. <sup>5</sup>CarMeN Laboratory, INSERM U1060, INRA U1397 Lyon, France. <sup>6</sup>Departments of Biochemistry, Medicine and Oncology, McGill University, Montreal, Quebec, Montreal, Canada. <sup>7</sup>These authors contributed equally: Nadine Martin, David Bernard. ✉email: [nadine.martin@lyon.unicancer.fr](mailto:nadine.martin@lyon.unicancer.fr); [david.bernard@lyon.unicancer.fr](mailto:david.bernard@lyon.unicancer.fr)

## RESULTS

### Mevalonate pathway promotes cellular senescence

In order to investigate whether the MVA pathway can regulate senescence, we expressed in MRC5 normal human fibroblasts a constitutively active PMVK<sup>37</sup> and its K22M mutant, a mutant reported to have lost its kinase activity<sup>38</sup>, to examine whether the kinase activity of PMVK is required to induce premature senescence (Fig. 1a, b and Supplementary Fig. 1A, B). We confirmed that K22M mutant did not display any kinase activity showing that it was indeed a PMVK kinase-dead mutant (PMVKmut) (Supplementary Fig. 1C). We also expressed an shRNA directed against PMVK (shPMVK) to examine the role of the MVA pathway in two relevant pro-senescence contexts, namely replicative senescence that occurs when replicative limit has been reached and progerin-induced premature senescence when compared to expression of non-mutated lamin A (Fig. 1a, b and Supplementary Fig. 1A, B). Progerin, a protein driving Hutchinson-Gilford progeria syndrome (HGPS), is encoded by the *LMNA* mutated gene. Progerin corresponds to a truncated prelamin A that is unable to be processed in a mature lamin A perturbing nuclear envelope and cell homeostasis and leading to premature senescence<sup>39</sup>. Remarkably, the constitutive overexpression of PMVK, but not the kinase-dead mutant PMVK, led to decreased cell proliferation (Fig. 1c, d). Most importantly, the knockdown of PMVK was sufficient to extend the replicative potential of normal human fibroblasts over successive passages (Fig. 1c, d) and expressing progerin, when compared to lamin A (Supplementary Fig. 1D, E). The overexpression of PMVK, but not its kinase-dead version, was also associated with the induction of key markers of cellular senescence: senescence-associated  $\beta$ -galactosidase (SA- $\beta$ -gal) activity (Fig. 1e) and increased mRNA levels of *p21<sup>CIP1</sup>* and SASP marker *IL-8* (Fig. 1f). On the contrary, decreasing PMVK reduced SA- $\beta$ -gal activity and decreased mRNA levels of *p21<sup>CIP1</sup>* and *IL-8* in normal fibroblasts at late passages (p36) (Fig. 1e, f) and expressing progerin (Supplementary Fig. 1F, G). Together these results show that PMVK contributes to replicative and progerin-induced senescence and its kinase activity participates in senescence regulation.

To further prove that this observed senescence is mediated by the MVA pathway and not the sole PMVK enzyme, we stably expressed a shRNA against PMVK and subsequently expressed the upstream enzyme MVK (Fig. 1a). As expected, constitutive overexpression of MVK (Supplementary Fig. 1H) induced premature cellular senescence, as shown by decreased cell density (Supplementary Fig. 1I, J), elevated SA- $\beta$ -gal activity (Supplementary Fig. 1K) and induction of both *p21<sup>CIP1</sup>* and *IL-8* mRNA levels (Supplementary Fig. 1L). Noteworthy, the knockdown of PMVK abolished MVK-induced premature senescence, rescuing decreased cell density (Supplementary Fig. 1I, J), and increased SA- $\beta$ -gal activity and *p21<sup>CIP1</sup>* and *IL-8* mRNA levels (Supplementary Fig. 1K, L).

Taken together, these data support that the MVA pathway plays a pivotal role in promoting cellular senescence.

### Dysfunctional mitochondria, ROS production, DNA damage and p53 mediate mevalonate pathway-induced senescence

p53 is a well-known critical effector of cellular senescence<sup>40</sup>. Its transcriptional targets such as *p21<sup>CIP1</sup>*, *GADD45A* and *GDF15* were upregulated at mRNA levels by the constitutive expression of PMVK (Fig. 2a) and their up-regulations were p53-dependent as they were prevented by p53 knockdown using siRNA (Fig. 2a), suggesting that p53 could mediate PMVK-induced senescence. Indeed, p53 knockdown in PMVK overexpressing cells (Supplementary Fig. 2A) reverted several features of senescence such as PMVK-induced p53 targets and *IL-8* mRNA expression (Fig. 2a), decrease in cell number (Fig. 2b) and increase in SA- $\beta$ -Gal activity (Fig. 2c).

During cellular senescence, p53 activation can occur through oxidative stress-induced DNA damage<sup>1</sup> and its subsequent DNA damage response<sup>2,3</sup>. Accordingly, p53 pathway activation upon PMVK constitutive expression resulted from increased oxidative stress - DNA damage pathway as cells overexpressing PMVK displayed increased DNA damage evidenced by increased  $\gamma$ H2AX positive cells (Fig. 2d), concomitantly with increased total ROS levels (Fig. 2e). Our results support that ROS is upstream of p53 as siRNA against p53 did not decrease ROS production (Supplementary Fig. 2B) whereas it decreased senescence (Fig. 2a–c) upon PMVK overexpression. Of note, cells overexpressing the kinase-dead mutant PMVK displayed a limited increase of  $\gamma$ H2AX positive cells and an absence of ROS generation (Fig. 2d, e). Importantly, NAC antioxidant treatment largely overcame PMVK-induced senescence (Fig. 2f–h) showing a critical role of ROS in mediating PMVK-induced senescence. In the context of replicative senescence, the sole knockdown of PMVK was sufficient to reduce  $\gamma$ H2AX positive cells and ROS levels (Supplementary Fig. 2C, D).

Mitochondria is one of the major sites of ROS production in the cell<sup>41</sup> and its dysregulation participates in cellular senescence<sup>13,19,42</sup>. Strikingly, constitutive overexpression of PMVK, but not of kinase-dead mutant PMVK, led to increased mitochondrial ROS generation as evidenced by enhanced intensity of specific mitochondrial ROS probe (Fig. 2i). In order to evaluate mitochondrial dysfunction in PMVK-expressing cells, we assessed mitochondrial membrane potential using cationic JC-1 dye<sup>43</sup>, but also mitochondrial oxygen consumption rate (OCR) through Seahorse mitochondrial stress test (Supplementary Fig. 2E)<sup>44</sup>. PMVK-induced cellular senescence is accompanied by a drop of mitochondrial membrane potential (Fig. 2j), which could be promoted by ROS production and/or increase ROS production, and a concomitant decrease of mitochondrial ETC functions, as evidenced by reduced mitochondrial basal, ATP-linked and maximal respiration (Fig. 2k and Supplementary Fig. 2E). Dysfunctional mitochondria may harbor changes in their morphology<sup>45,46</sup>. Related to mitochondrial dysfunction observed in PMVK-expressing cells, we also identified atypical and persistent enlarged morphology of mitochondria in PMVK-expressing cells using electron transmission micrographs (Fig. 2l).

All these results support that PMVK could promote senescence by dysregulating ETC mitochondrial functions, further inducing ROS production, DNA damage and p53 activation.

### The cholesterol biosynthetic branch participates in mevalonate pathway-induced senescence

Farnesyl-5-pyrophosphate is the end-product of the MVA pathway and presents three isoprene units, elementary units further used either to be transferred as prenyl groups to proteins or to be condensed into more complex poly-isoprenoids, that include among others dolichol, ubiquinone or cholesterol<sup>33</sup> (Fig. 3a). In order to dissect the role of downstream branches in the PMVK-induced senescence, we knocked down the first enzyme of each branch, subsequently overexpressed PMVK and automatically counted the number of cells 4 days later. Only the knockdown of FDFT1, the first enzyme of the cholesterol biosynthesis branch, partially reverted the decreased cell number induced by PMVK overexpression (Fig. 3a, b). siRNA-mediated FDFT1 knockdown (Supplementary Fig. 3A) also rescued PMVK-induced decrease in cell density (Fig. 3c), increase in SA- $\beta$ -gal activity (Fig. 3d), and increase in *p21<sup>CIP1</sup>* and *IL-8* mRNA levels (Fig. 3e), without impacting PMVK mRNA level (Supplementary Fig. 3A). Confirming these results, stable knockdown of FDFT1 by two independent shRNA partly reverted premature senescence induced by PMVK expression (Supplementary Fig. 3B–D). In line with a role of the cholesterol biosynthetic branch in inducing cellular senescence, the expression of PMVK, but not the kinase-dead mutant PMVK, boosted intracellular cholesterol content, according

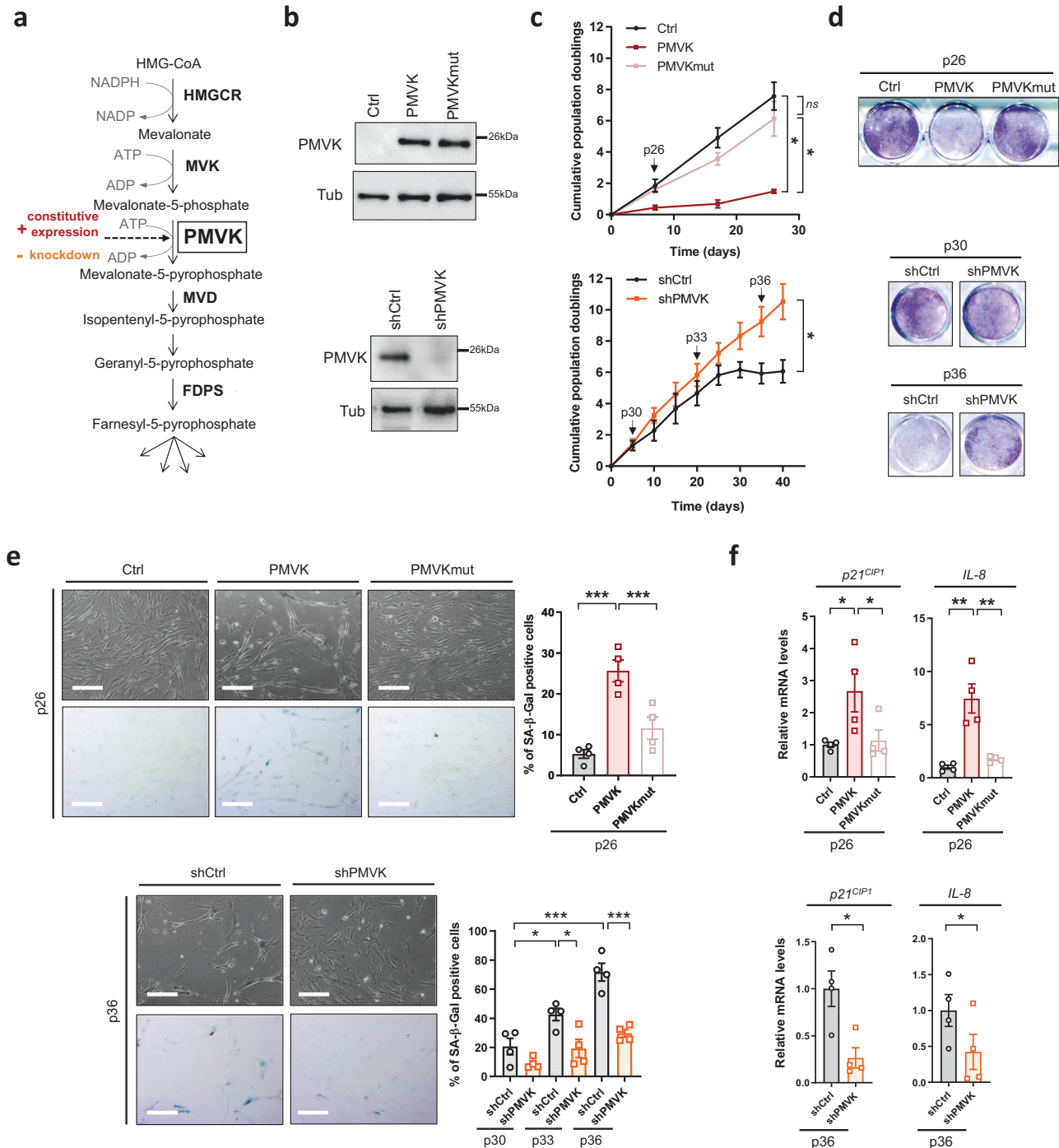
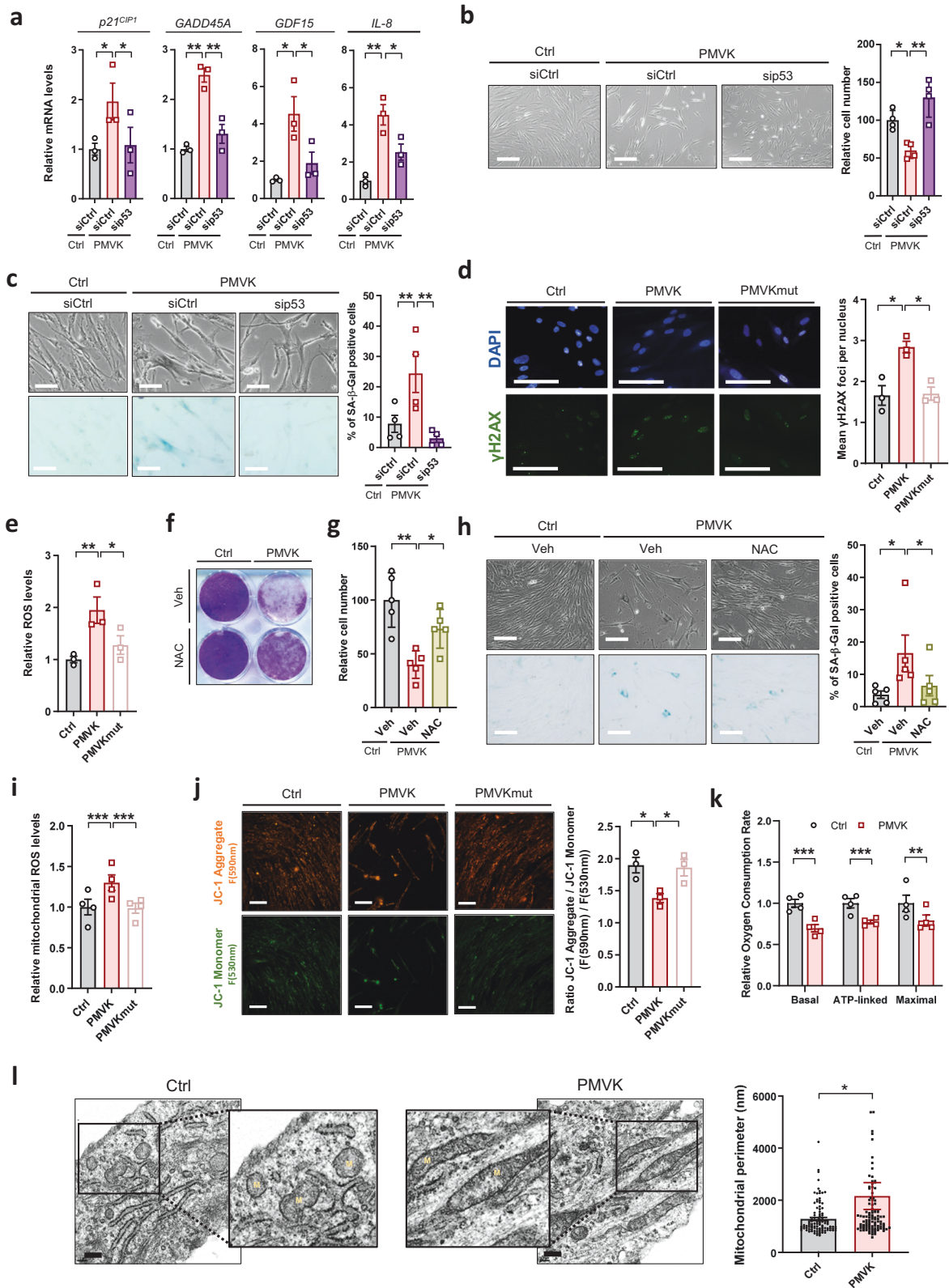


**Fig. 1 | The MVA pathway regulates cellular senescence in normal cells.** **a** Schematic representation of the MVA pathway in eukaryotic cells. HMGCR, HMG-CoA reductase; MVK, mevalonate kinase; PMVK, phosphomevalonate kinase; MVD, mevalonate-diphosphate decarboxylase; FDPS, farnesyl diphosphate synthase. Constitutive expression (in red) or knockdown by shRNA (in orange) was performed in MRC5 fibroblasts. **b** Relative PMVK and Tubulin protein levels in empty vector (Ctrl), PMVK- or Kinase Dead (PMVKmut) PMVK-expressing cells and in shCtrl- or shPMVK-expressing cells. **c** Growth curves of Ctrl, PMVK- or PMVKmut-expressing cells, and shCtrl and shPMVK-expressing cells. Mean  $\pm$  SEM of  $n = 4$  independent biological replicates. RM one-way ANOVA test on last time point. **d** Crystal violet staining of Ctrl, PMVK- or PMVKmut-expressing cells at early passage (p26), and of shCtrl- and shPMVK-expressing cells at early (p30) and late (p36) passage. **e** Micrographs and quantification of SA- $\beta$ -gal positive cells of Ctrl, PMVK- or PMVKmut-expressing cells at early passage (p26), and of shCtrl- and shPMVK-expressing cells during passages. Mean  $\pm$  SEM of  $n = 4$  independent biological replicates. Scale bar: 100  $\mu$ m. RM one-way ANOVA test (upper panel) and paired Student's T-test (lower panel). **f** RT-qPCR of *p21<sup>CIP1</sup>* and *IL-8* genes in Ctrl, PMVK- or PMVKmut-expressing cells at early passage (p26), and of shCtrl- and shPMVK-expressing cells at late passage (p36). Mean  $\pm$  SEM of  $n = 4$  independent biological replicates. RM one-way ANOVA test (upper panel) and paired Student's T-test (lower panel). ns (nonsignificant); \* $p < 0.05$ ; \*\* $p < 0.01$ ; \*\*\* $p < 0.001$ ).



to the fluorescence of the cholesterol sensor filipin<sup>47</sup> (Fig. 3f), and increased cholesterol-dependent LXR transcriptional targets<sup>48</sup>, namely *ABCA1* and *ABCG1* (Fig. 3g).

Altogether these results indicate a functional role of the cholesterol biosynthesis pathway in the regulation of PMVK-induced senescence.

**Fig. 2 MVA pathway induction promotes mitochondrial dysfunction, ROS accumulation, DNA damage and p53-dependent senescence.** **a** RT-qPCR of p53-regulated genes, including *p21<sup>Cip1</sup>*, *GADD45A*, *GDF15* and *IL-8* in Ctrl or PMVK-expressing cells previously transfected with control non-targeting siRNA (siCtrl) or p53-targeted siRNA (sip53). Mean  $\pm$  SEM of  $n = 3$  independent biological replicates. RM one-way ANOVA test. **b** Micrographs of Ctrl and PMVK-expressing cells upon sip53. Quantification of relative cell number in Ctrl and PMVK-expressing cells. Mean  $\pm$  SEM of  $n = 4$  independent biological replicates. Scale bar: 100  $\mu$ m. RM one-way ANOVA test. **c** Representative micrographs and quantification of SA- $\beta$ -gal positive cells in Ctrl and PMVK-expressing cells upon siCtrl or sip53. Mean  $\pm$  SEM of  $n = 4$  independent biological replicates. Scale bar: 50  $\mu$ m. RM one-way ANOVA test. **d** Micrographs of Ctrl, PMVK- or PMVKmut-expressing cells immunostained with  $\gamma$ H2AX antibody and DAPI stained. Scale bar: 10  $\mu$ m. Number of  $\gamma$ H2AX foci were counted manually using Fiji and divided by the number of nuclei to evaluate the mean number of foci per nucleus. Fully stained nuclei were excluded from this analysis. Mean  $\pm$  SEM of  $n = 3$  independent biological replicates. RM one-way ANOVA test. **e** Quantification of relative ROS levels using CellROX™ Green Reagent probe and measuring its fluorescence intensity in Ctrl, PMVK- and PMVKmut- expressing cells. Mean  $\pm$  SEM of  $n = 3$  independent biological replicates. RM one-way ANOVA test. **f** Crystal violet staining after 8 days in Ctrl and PMVK-expressing cells upon vehicle (Veh) or N-acetyl-cysteine (NAC) antioxidant treatment. **g** Cell count in Ctrl and PMVK-expressing cells upon vehicle or NAC treatment. Mean  $\pm$  SEM of  $n = 5$  independent biological replicates. RM one-way ANOVA test. **h** Representative micrographs and quantification of SA- $\beta$ -gal positive cells in Ctrl and PMVK-expressing cells upon the vehicle or NAC treatment. Mean  $\pm$  SEM of  $n = 5$  biological replicates. Scale bar: 10  $\mu$ m. RM one-way ANOVA test. **i** Quantification of mitochondrial ROS using mitochondrial hydroxyl radical detector and measuring its fluorescence intensity in Ctrl, PMVK-, and PMVKmut-expressing cells. Mean  $\pm$  SEM of  $n = 4$  independent biological replicates. RM one-way ANOVA test. **j** Mitochondrial membrane polarisation measurement assessed by JC1-probe. Representative micrographs of JC1 in both monomer (F530 nm)-green) or aggregate (F590 nm)-orange) forms within Ctrl, PMVK-, and PMVKmut-expressing cells. Scale bar: 100  $\mu$ m. Quantification of ratio fluorescence intensity (Monomer) / fluorescence intensity (Aggregate). Mean  $\pm$  SEM of  $n = 3$  independent biological replicates. RM one-way ANOVA test. **k** Seahorse quantitative analysis of relative oxygen consumption rate (OCR). Basal OCR was evaluated in resting conditions, ATP-linked OCR upon Oligomycin treatment and Maximal OCR upon FCCP treatment. Mean  $\pm$  SEM of  $n = 5$  independent biological replicates. Multiple paired Student's T-tests. **l** Representative electron micrographs of mitochondria in Ctrl and PMVK-expressing cells and quantification of mitochondrial perimeters. M: Mitochondria. Mean  $\pm$  SD of  $n = 103$  (Ctrl) and  $n = 106$  (PMVK) mitochondria. Representative of  $n = 3$  independent biological experiments. Scale bar: 300 nm. (\* $p < 0.05$ ; \*\* $p < 0.01$ ; \*\*\* $p < 0.001$ ).

### Mitochondrial master regulator Estrogen-Related receptor alpha mediates mevalonate pathway-induced senescence

Estrogen-Related Receptor alpha (ERR $\alpha$  or NR3B1) is a key regulator of mitochondrial functions and of metabolism<sup>49,50</sup>. Noteworthy, mRNA levels of ERR $\alpha$  were upregulated in both replicative and progerin-induced senescence (Supplementary Fig. 4A). We then assessed during PMVK-induced senescence the expression of ERR $\alpha$  targets: ERR $\alpha$  itself<sup>51</sup> encoded by *ESRRA* gene and *UQCRFS1*, *NDUF5A*, *SDHA* and *SDHB* nuclear-encoded mitochondrial targets<sup>49</sup>. The constitutive overexpression of PMVK increased the expression of *ESRRA*, *UQCRFS1*, *NDUF5A*, *SDHA* and *SDHB* (Fig. 4a, b and Supplementary Fig. 4B, C). Remarkably, this ERR $\alpha$  program upregulation was partly reverted by the knockdown of *FDFT1* (Fig. 4c, d and Supplementary Fig. 4B–D) suggesting the hypothesis of ERR $\alpha$  activation by the cholesterol biosynthetic pathway during PMVK-induced senescence. Further confirming an activation of ERR $\alpha$  during PMVK-induced senescence, its knockdown by siRNA strategy blocked PMVK-induced upregulation of various ERR $\alpha$  targets (Supplementary Fig. 4E, F), without impacting PMVK levels (Supplementary Fig. 4G).

We next sought to determine whether cholesterol-dependent ERR $\alpha$  program functionally mediates the PMVK-induced senescence. Knockdown of ERR $\alpha$  in PMVK-overexpressing cells partially rescued the decreased cell number (Fig. 4e, f), the increased SA- $\beta$ -gal activity (Fig. 4g), and the elevated *p21<sup>Cip1</sup>* and *IL-8* mRNA levels (Fig. 4h). Further supporting that ERR $\alpha$  mediates MVA/cholesterol biosynthetic pathway-induced senescence, its chemical inhibition using XCT-790 compound, similarly to ERR $\alpha$  knockdown, largely bypassed senescence induced by PMVK expression according to growth curves and SA- $\beta$ -Gal activity (Supplementary Fig. 4H, I).

To next investigate the relevance of these discoveries in a relevant pathophysiological system, we investigated the level of cellular senescence in the liver of ERR $\alpha$  knockout mice fed by high-fat diet (HFD), known to increase cholesterol levels and drive cellular senescence and senescence-dependent steatosis<sup>27,52</sup>. ERR $\alpha$  target genes *Uqcrfs1*, *Nduf5a*, *Sdha* and *Sdhb* were only slightly induced by the HFD, potentially because some endogenous ERR $\alpha$  activity upon the chow diet and were accordingly reduced at mRNA levels in the liver of ERR $\alpha$  knockout mice, especially upon HFD (Supplementary Fig. 4J). As expected, HFD resulted in the accumulation of senescence markers such as

*p21<sup>Cip1</sup>* (Fig. 4i, j), *Gadd45a* and *Gdf15* p53 targets (Fig. 4j), *Mmp12* SASP factor (Fig. 4k), and pro-inflammatory SASP factors *Cxcl1* and *Cxcl2* (Fig. 4k), which are murine functional orthologs of human *IL8*<sup>53</sup>. Strikingly, increase in the expression of these senescence markers was abrogated in liver of ERR $\alpha$  knockout mice upon HFD (Fig. 4i–k). As previously reported<sup>54</sup>, HFD-fed ERR $\alpha$  knockout mice did not display hepatic steatosis, a process tightly linked to senescent cell accumulation<sup>27,52</sup>. Examination of the same senescence markers in white adipose tissue (WAT), which can display increased senescence during HFD<sup>55</sup>, displayed some similarities and differences with the liver. Indeed, *p21<sup>Cip1</sup>*, *Gdf15*, *Mmp12*, and *Cxcl2* were induced whereas *Gadd45a* and *Cxcl1* were not in the control mice by the HFD (Supplementary Fig. 4K). Induction by the HFD of *Gdf15*, *Mmp12*, *Cxcl2* was decreased in the ERR $\alpha$  knockout mice (Supplementary Fig. 4K).

Overall, these results highlight the importance of ERR $\alpha$  in mediating MVA/cholesterol biosynthetic pathway-induced cellular senescence in vitro in human cells and in vivo in mouse.

### DISCUSSION

In this study, we deciphered the role of the MVA pathway, the cholesterol biosynthetic pathway and of ERR $\alpha$  transcription factor in mediating cellular senescence. MVA pathway activation triggers premature senescence whereas its inhibition delays replicative and progerin-induced senescence in normal human cells. PMVK-induced senescence seems to mediate, at least partly, by the biosynthetic cholesterol pathway and the activation of an ERR $\alpha$  transcriptional program, mitochondrial ROS accumulation, DNA damage and p53 activation. ERR $\alpha$  is also mediating cellular senescence in the liver, and to a lower extent in the WAT, when mice are subjected to a high fat diet (Fig. 5).

Several studies depicted a role of MVA pathway in cellular senescence through the use of statins and aminobisphosphonates inhibitors but with conflicting conclusions. For instance blocking the MVA pathway with these inhibitors has been shown to delay senescence in HUVEC model<sup>34</sup>, whereas it promotes senescence in oral keratinocytes and has no obvious effect in oral fibroblasts<sup>35</sup>. Besides, statins and aminobisphosphonates have been shown both to blunt SASP, notably pro-inflammatory cytokines including IL-6, IL-8 and monocyte chemoattractant protein (MCP)-1<sup>56–59</sup>, and some of its effects, including pro-tumorigenic activity<sup>60</sup>.

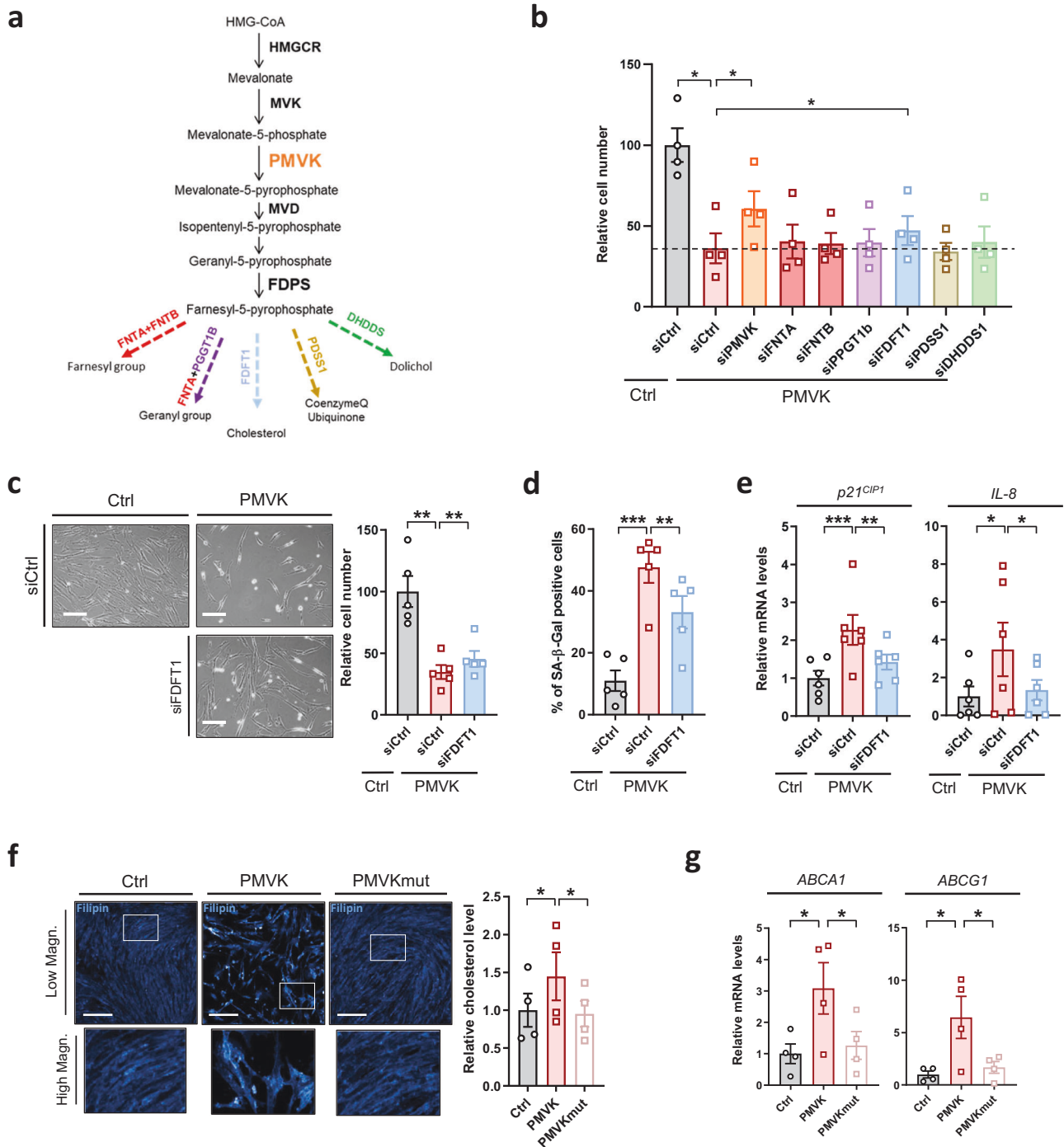


**Fig. 3 Cholesterol biosynthetic branch participates in PMVK-induced senescence.** **a** Schematic representation of the MVA pathway and subbranches stemming from Farnesyl-5-Pyrophosphate, including farnesylation (red), geranylation (purple), cholesterol synthesis (blue), ubiquinone synthesis (gold) and dolichol biosynthesis (green). First specific enzymes of each subbranch are indicated. **b** Quantification of number of cells after transfection with siRNA against PMVK and enzymes of downstream subbranches of the MVA pathway in PMVK-expressing cells. Mean  $\pm$  SEM representative of  $n = 4$  independent biological replicates. RM one-way ANOVA test. **c** Representative micrographs of Ctrl and PMVK-expressing cells upon siCtrl or siFDFT1 transfection (scale bar: 100  $\mu$ m) and cell number quantification. Mean  $\pm$  SEM of  $n = 5$  independent biological replicates. RM one-way ANOVA test. **d** Quantification of SA- $\beta$ -gal positive cells in Ctrl- and PMVK-expressing cells upon siCtrl or siFDFT1 transfection. Mean  $\pm$  SEM of  $n = 5$  independent biological replicates. RM one-way ANOVA test. **e** RT-qPCR of *p21<sup>CIP1</sup>* and *IL-8* genes in Ctrl and PMVK-expressing cells upon siCtrl or siFDFT1 transfection. Mean  $\pm$  SEM of  $n = 6$  independent biological replicates. RM one-way ANOVA test. **f** Cholesterol assay using filipin fluorescent sensor in Ctrl, PMVK-, and PMVKmut-expressing cells. Scale bar: 150  $\mu$ m. Relative quantification of intracellular cholesterol level. Mean  $\pm$  SEM of  $n = 4$  independent biological replicates. RM one-way ANOVA test. **g** RT-qPCR against *ABCA1* and *ABCG1* genes in Ctrl, PMVK-, and PMVKmut-expressing cells. Mean  $\pm$  SEM of  $n = 3$  independent biological replicates. RM one-way ANOVA test. (\* $p < 0.05$ ; \*\* $p < 0.01$ ; \*\*\* $p < 0.001$ ).

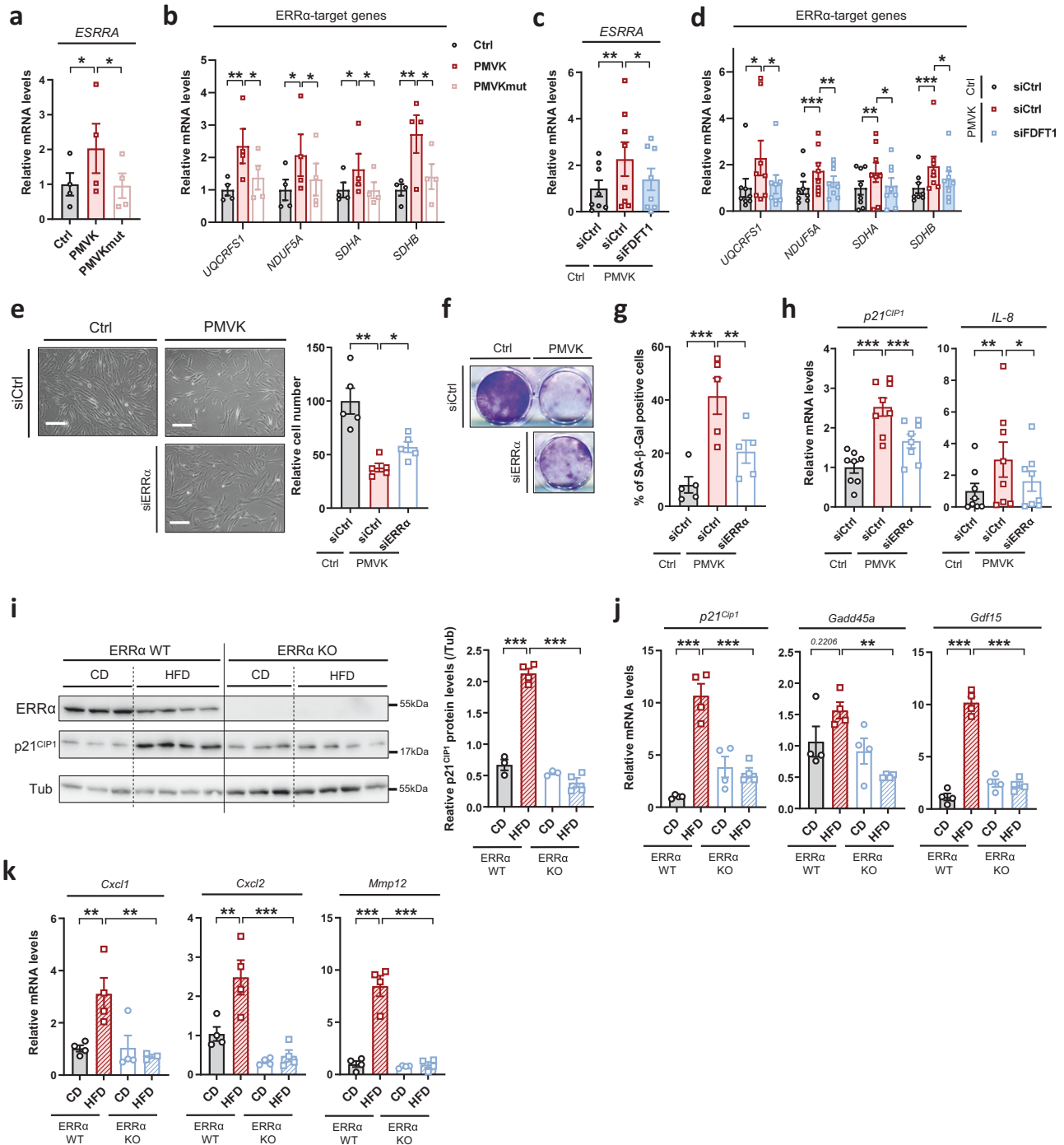


**Fig. 4** Mitochondrial master regulator Estrogen-Related Receptor alpha mediates PMVK-induced senescence. **a, b** RT-qPCR of *ESRRA* and ERR $\alpha$  target genes (including *UQCRCF1*, *NDUF5A*, *SDHA*, *SDHB*) in empty vector (Ctrl), PMVK- or Kinase Dead (PMVKmut) PMVK-expressing cells. Mean  $\pm$  SEM of  $n = 4$  independent biological replicates. RM one-way ANOVA test. **c, d** RT-qPCR of *ESRRA* and ERR $\alpha$  target genes in Ctrl and PMVK-expressing cells, upon siCtrl or siERR $\alpha$  transfection. Mean  $\pm$  SEM of  $n = 8$  independent biological replicates. RM one-way ANOVA test. **e** Representative micrographs and cell number quantification of Ctrl and PMVK-expressing cells previously transfected with siERR $\alpha$ . Scale bar: 100  $\mu$ m. Mean  $\pm$  SEM of  $n = 5$  independent biological replicates. RM one-way ANOVA test. **f** Crystal violet staining of Ctrl and PMVK-expressing cells previously transfected with siERR $\alpha$ . **g** Quantification of SA- $\beta$ -gal positive cells in Ctrl and PMVK-expressing cells upon siERR $\alpha$  transfection. Mean  $\pm$  SEM of  $n = 5$  independent biological replicates. RM one-way ANOVA test. **h** RT-qPCR of *p21<sup>CIP1</sup>* and *IL-8* genes in Ctrl and PMVK-expressing cells previously transfected with siCtrl or siERR $\alpha$ . Mean  $\pm$  SEM of  $n = 7$  independent biological replicates. RM one-way ANOVA test. **i** Western blot on ERR $\alpha$ , p21<sup>CIP1</sup> and Tubulin in liver of ERR $\alpha$  WT and ERR $\alpha$  KO male mice fed either by chow diet (CD) or high-fat diet (HFD). Quantification of p21<sup>CIP1</sup> levels normalized to Tubulin levels. Mean  $\pm$  SEM of  $n = 3-4$  male mice. Ordinary one-way ANOVA test. **j, k** RT-qPCR of p53 target genes (namely *p21<sup>CIP1</sup>*, *Gadd45a*, *Gdf15*) and SASP members *Cxcl1*, *Cxcl2* and *Mmp12* genes in liver of ERR $\alpha$  WT and ERR $\alpha$  KO male mice fed either by chow diet (CD) or high-fat diet (HFD). Mean  $\pm$  SEM of  $n = 3-4$  mice. Ordinary two-way ANOVA test. (\* $p < 0.05$ ; \*\* $p < 0.01$ ; \*\*\* $p < 0.001$ ).

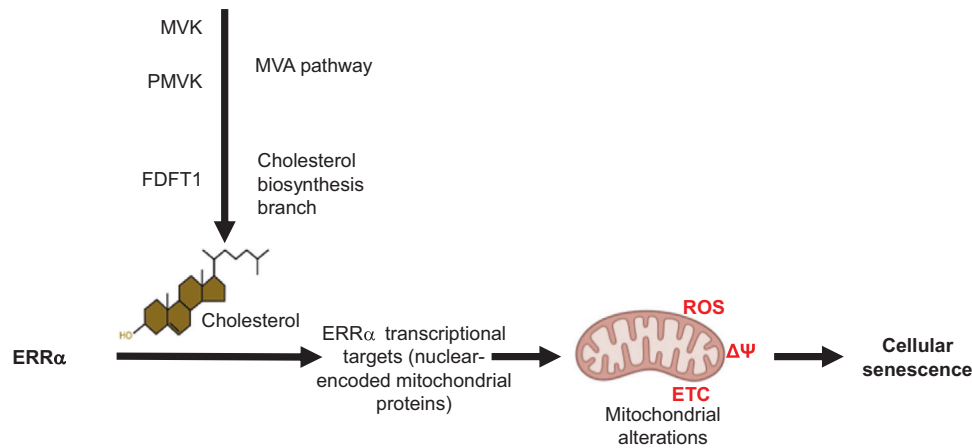


**Fig. 5 A key role for cholesterol-ERR $\alpha$  axis in promoting cellular senescence.** The experimental models, human cells through manipulating the MVA pathway or WT or ERR $\alpha$  KO mice subjected or not to a HFD (high-fat diet), indicate that cholesterol accumulation triggers ERR $\alpha$  activation. In both in vitro and in vivo conditions, ERR $\alpha$  is determinant to mediate the subsequent cellular senescence phenotype. Mechanistically demonstrated in vitro, the upregulation of ERR $\alpha$  target genes enhances mitochondrial dysfunction, through electron transport chain (ETC) alteration, drop in mitochondrial membrane potential ( $\Delta\Psi$ ) and ROS production, ultimately resulting in cellular senescence.

Dampening SASP through statins could explain their numerous anti-inflammatory outcomes in vivo<sup>61,62</sup>. Our results using genetic tools, knockdown and/or overexpression of PMVK or MVK, clearly demonstrate that the MVA pathway promotes cellular senescence and associated SASP in normal human fibroblasts. Discrepancies with pharmacological studies might thus result from the known pleiotropic effects of the MVA inhibitors, as these inhibitors were found to exert multiple MVA pathway-independent actions<sup>63,64</sup>. For instance, bisphosphonates in addition to inhibiting FDPS enzyme and downstream pathway also induce accumulation of the upstream metabolite isopentenyl diphosphate (IPP) which can induce apoptosis, at least in some specialized cells<sup>57</sup>.

Although the MVA pathway contributes to senescence as its knockdown delays replicative and progerin-induced senescence, how its activity is regulated during senescence remains unknown. PMVK is up-regulated during progerin-induced senescence but not during replicative senescence, with the same trends for FDFT1, whereas MVK levels are not modified (Supplementary Fig. 5A, B). Nonetheless, cholesterol levels are increased during both replicative or progerin-induced senescence (Supplementary Fig. 5C, D). Taken together, these results suggest an accumulation of cholesterol in senescent cells, in line with two recent studies displaying this accumulation in other senescence models<sup>65,66</sup>, and that this accumulation is not directly due to an up-regulation of PMVK and FDFT1. We can then speculate that post-translational modifications, as previously reported with two upstream MVA enzymes, namely HMGCR phosphorylation<sup>67</sup> or HGMCS sumoylation<sup>68</sup>, are involved in regulating the MVA pathway during senescence. Last but not least, cholesterol level is regulated not only by synthesis but also through transport and/or degradation<sup>69</sup>. Thus, the exact contribution of MVA pathway in the accumulation of cholesterol in these senescence models would further require deeper investigations.

Our results suggest an unexpected link between the MVA pathway and the DNA damage/p53 pathway, a well-known effector pathway promoting cellular senescence<sup>70</sup>. This DNA damage/p53 pathway could be activated by an oxidative stress upon PMVK-induced senescence, probably mainly provoked by increased mitochondrial ROS production. Mitochondrial ROS are well known mediators of cellular senescence and can result from multiple mitochondrial alterations, from increased respiration and thus increased basal electron leaks during the electron transport chain activity, to decreased respiration but increased levels of electron leaks because of altered electron transport chain complex

associations<sup>41</sup>. According to our findings, PMVK-induced senescence results in decreased respiration with increased mitochondrial ROS production. This is in line with previous results showing that maladaptive complex 1 assembly through increased transcriptional program of ETC components results in decreased respiration with increased mitochondrial ROS and promotes cellular senescence and aging<sup>71</sup>.

Our siRNA approach to reveal which sub-branch(es) of the MVA pathway participate in PMVK-induced senescence identified an involvement of the cholesterol biosynthetic branch. Of note, this finding does not exclude that some other sub-branches could collaborate with the cholesterol biosynthetic pathway to regulate cellular senescence. Beyond the specific role of ceramide<sup>24</sup>, little is known about links between lipids and senescence except that the lipid metabolism is largely modified in senescent cells. In particular and in accordance with our results in replicative and progerin-induced senescence, it has been reported that free fatty acids and cholesterol levels are increased in senescent cells<sup>25,26,28,29</sup> and that ceramides or prostaglandins regulate also the onset of senescence<sup>24,72</sup>. In line with our findings, recent articles reported an upregulation of the expression of cholesterol synthesis genes in a model of oncogene-induced senescence<sup>73</sup> and an increased cholesterol during DNA damage-induced senescence<sup>66</sup>. During OIS, knockdown of some cholesterol synthesis genes partially bypassed cell proliferation arrest. However, the mechanisms behind these observations were not deciphered<sup>73</sup>. During DNA damage-induced senescence, cholesterol is thought to promote the SASP by increasing mTORC1 activity<sup>66</sup>. Our results underline the importance of cholesterol biosynthetic branch downstream of the MVA pathway in the regulation of cellular senescence and allow us to propose a mechanistic model through ERR $\alpha$  activation. Our findings and the findings of others do not exclude additional mechanisms, dependent or not on ERR $\alpha$ , controlled by the cholesterol in cellular senescence, including in a paracrine manner, as it has been described for some other lipids<sup>74</sup>.

Our results support that ERR $\alpha$  participates in the pro-senescence function of the cholesterol biosynthetic pathway as its knockdown or its chemical inhibition partially overcomes PMVK-induced premature senescence. Although ablation of FDFT1, ERR $\alpha$  or p53 decrease PMVK-induced senescence, their effects show slight differences and not complete reversal of the phenotype suggesting that other factors and pathways could also contribute to PMVK-induced senescence. A previous study proposed that cholesterol can be an ERR $\alpha$  ligand<sup>50</sup>, as this is still



largely debated further investigation will be needed to confirm or not this observation. As far as we know ERR $\alpha$  has not been associated with cellular senescence. Nevertheless, it has been shown to be activated during cancer cell death in response to PLA2R1/JAK/STAT signalling, this signalling being known to promote cellular senescence in normal human cells and in mice<sup>58,75–77</sup>. In cancer cells, PLA2R1/JAK/STAT signalling in an ERR $\alpha$ -dependent manner blocks mitochondrial respiration, alters mitochondria and mediates ROS generation<sup>78</sup>, reminiscent to the observed alterations during PMVK-induced senescence in normal cell.

We have previously reported that ERR $\alpha$ -null mice are protected from HFD-induced non-alcoholic fatty liver disease (NAFLD)<sup>54</sup>, which is characterized by liver steatosis. Senescent cells accumulate in the liver during HFD and/or aging and contribute to liver steatosis<sup>27,52</sup>. We observed that ERR $\alpha$ -depleted livers are protected from increased senescence, suggesting that reduced ERR $\alpha$ -induced senescence could contribute to the decreased steatosis in the liver of these mice<sup>54</sup>. Adding another layer of complexity, body weight (BW) is decreased in ERR $\alpha$  KO mice upon HFD<sup>54</sup>, suggesting that BW decrease could contribute to decrease senescence and steatosis observed in the liver of these mice. As far as we know whether senescent cell accumulation can impact BW is currently unknown. Further studies will thus be needed to better define the complex functional connection between BW, senescence and steatosis. Still, mechanistically, it has been previously shown that ERR $\alpha$  loss<sup>54</sup> or elimination of senescent cells<sup>27</sup> results in change in free fatty acid metabolism decreasing liver steatosis. Beyond these observations highlighting the importance of ERR $\alpha$  in regulating senescence and senescence-dependent liver steatosis, we can speculate that other known pathophysiological processes regulated by ERR $\alpha$  could rely on its effect on cellular senescence. For instance, our results in WAT also support a decreased cellular senescence in the ERR $\alpha$ -null mice. ERR $\alpha$ -null mice display reduced osteoporosis in female mice<sup>79,80</sup> and cellular senescence in the bone is known to promote osteoporosis<sup>81</sup>, suggesting that ERR $\alpha$ -promoted senescence could participate in ERR $\alpha$ -induced osteoporosis. In the same line, antiosteoporosis effects of MVA pathway inhibitors, aminobisphosphonates, are well-known<sup>82</sup> and may partly rely on reduced ERR $\alpha$  activity, though further studies need to critically test this hypothesis. Effect of ERR $\alpha$  in vivo on senescence can then be wide in term of tissue physiology impacted and then still needs to be deeply investigated in the future. For instance, ERR $\alpha$  is expressed in different cell types in the mouse liver, according to publicly available single-cell RNA sequencing, raising the question of the cells impacted by ERR $\alpha$  on senescence occurrence during HFD. In the context of ERR $\alpha$ -driven cellular senescence in vivo, it will also be critical to characterize mitochondrial phenotype in tissue as our results support it is a critical mediator of MVA pathway/ERR $\alpha$ -induced senescence.

Overall, our results emphasize MVA pathway/cholesterol biosynthetic pathway, cholesterol levels and subsequent ERR $\alpha$  program as a new pathway regulating cellular senescence. As impacting cellular senescence has attracted many interests to improve various age-related diseases and health span<sup>7–9</sup>, our work paves the way to new potential senotherapeutic strategies using drugs targeting the mevalonate pathway (statins, bisphosphonates) and in particular PMVK, and ERR $\alpha$ .

## METHODS

### Cell culture and reagents

MRC5 normal human fibroblasts (ATCC, Manassas, VA, USA), and kidney 293 GP cells (Clontech, Mountain View, CA, USA) were cultured in Dulbecco's modified Eagle's medium (DMEM, Life Technologies, Carlsbad, USA) with GlutaMax and supplemented

with 10% FBS (Sigma-Aldrich, Saint-Louis, USA) and 1% penicillin/streptomycin (ThermoFisher Scientific). XCT-790 (Medchem, HY-10426/CS-2413) was used at 150 nM. N-Acetyl-Cysteine (NAC) (A9165, Sigma-Aldrich) was used directly after infection at 1 mM. These compounds were renewed every two days.

### Vectors, transfection and infection

Retroviral vectors were used to constitutively overexpress MVK, PMVK, lamin A and progerin. MVK and PMVK plasmids were provided by Addgene in the Myristoylated Kinase Library (Kit #1000000012) described in<sup>37</sup>. K22M mutation of the kinase-dead PMVK mutant (PMVKmut) was generated using QuickChange Site-Directed Mutagenesis Kit (Agilent, Catalog # 200518). pBABE-puro-GFP-wt-lamin A (Addgene #17662) and pBABE-puro-GFP-progerin (Addgene #17663) were described in<sup>83</sup>. Lentiviral particles were used to constitutively express shPMVK (pLV[shRNA]-Hygro-U6>hPMVK[shRNA#4], Target sequence: GAGAACCTGATAGAATTTATC) and shFDFT1 (pLV[shRNA]-Hygro-U6 > hFDFT1[shRNA#2], Target sequence CAACGATCTC CCTTGAGTTTA and pLV[shRNA]-Hygro-U6 > hFDFT1[shRNA#3], Target sequence: ACC ATTTGAATGTTCCG-TAATA) and were provided by VectorBuilder. 293 T or 293GP virus-producing cells were transfected using the GeneJuice reagent according to the manufacturer's recommendations (Merck Millipore). Two days after transfection, viral supernatant was collected, diluted with fresh medium (1/2) and hexadimethrine bromide was added (final concentration 8  $\mu$ g/mL; Sigma-Aldrich). Target cells were then infected, centrifugated with virus particles for 30 min at 2000 rpm and subsequently incubated during 6 h at 37 °C 5% CO<sub>2</sub>. Fresh medium was added after 6 h incubation. One day later, infected cells were selected with Geneticin at 75  $\mu$ g/mL, Hygromycin at 15  $\mu$ g/mL (ThermoFisher Scientific), or puromycin at 500 ng/ml (Invivogen).

### siRNA

MRC5 fibroblasts were plated and reverse transfected with ON-TARGET plus SMART pool of small interference (si) RNAs: siCtrl (Catalog: D-001810-10-20 / Lot#2693147), siPMVK (Catalog: L-006782-00), siFNTA (Catalog: L-008807-00), siFNTB (Catalog: L-010093-00), siPGGT1B (Catalog: L-008703-00), siFDFT1 (Catalog: #L-009442-00-0005 / Lot#180518), siPDSS1 (Catalog: L-008464-01), siDHDDS (L-010399-01), siESRRA (Catalog: #L-003403-00-0005 / Lot#191211), sip53 (Catalog: #L-003329-00-0001) / Lot#180912) (Horizon Discovery) previously incubated for 20 min with Dharmafect 1 Transfection Reagent (Horizon Discovery) 0,6% in antibiotics- and serum-free medium DMEM with GlutaMax. Final siRNA concentration in the well was 15 nM. The day after, cells were infected (with retroviral particles containing PMVK) as referenced previously.

### Animals

Wild-type (WT) and ERR $\alpha$ <sup>-/-</sup> male mice in a C57BL/6J genetic background were housed and fed ad libitum with free access to water in an animal facility at McGill University. All animal experiments were conducted in accord with accepted standards of humane animal care and all protocols were approved by the McGill Facility Animal Care Committee and the Canadian Council on Animal Care. For high-fat diet (HFD) experiments, mice were separated randomly into groups of two to three mice per cage and fed either a control chow diet consisting of 10 kcal percent fat (catalog no. TD.08806; Harlan, Indianapolis, IN) or an HFD consisting of 60 kcal percent fat (catalog no. TD.06414; Harlan) and known to increase cholesterol levels according to manufacturer, during 15 weeks, initiated at 6 weeks of age. For all mouse experiments, littermates were used and mice were euthanized by cervical dislocation at Zeitgeber time (ZT) 4 for tissue isolations.

### RNA extraction, reverse transcription, and real-time quantitative PCR

Total RNAs were extracted with phenol-chloroform using Upzol (Dutscher, Brumath, France). Synthesis of cDNA was performed using Maxima First cDNA Synthesis Kit (ThermoFisher Scientific) from 1 µg of total RNA. cDNA (50 ng/µL) was used as a template for quantitative PCR (qPCR), and mixed with primers (200 nM), SYBR™ Green PCR Master Mix (ThermoFisher Scientific) or TaqMan mix (Roche) and Universal Probe Library probes (100 µM) (ThermoFisher Scientific) for the gene of interest. Reactions were performed in triplicate. qPCR analyses were carried out with the FX96 Thermocycler (Biorad, Hercules, USA). Relative mRNA levels were calculated using the Comparative Ct ( $\Delta\Delta\text{CT}$ ) method. Gene expression was normalized with *hACTB* or *mRplp*. Primer sequences used are listed in Supplementary Table 1.

### Senescence-associated $\beta$ -Galactosidase analysis and Crystal violet

For SA- $\beta$ -Galactosidase assay, cells were washed with PBS 1X, fixed for 5 min in 2% formaldehyde / 0.2% glutaraldehyde, rinsed twice in PBS 1X, and incubated at 37 °C overnight in SA- $\beta$ -Galactosidase staining solution as previously described<sup>84</sup>. For crystal violet staining, cells were washed with PBS 1X, fixed for 15 min in 3.7% formaldehyde and stained with crystal violet.

### ROS and JC1 quantification

Total cellular and specific mitochondrial ROS were measured respectively with CellROX™ Green Reagent (ThermoFisher Scientific) and Cell Meter™ Mitochondrial Hydroxyl Radical Detection Kit (ATT Bioquest) according to manufacturer's recommendations. For JC1, JC1-Mitochondrial Membrane Potential Assay Kit (ab113850, Abcam) was used. JC1 monomers and aggregates were both excited at 488 nm. Detection of fluorescence for JC1 monomers and aggregates were performed respectively at 530 nm and 590 nm. Ratio F(aggregate)/F(monomer) was subsequently evaluated. Pictures acquisition was performed using Operetta CLS High-Content Analysis System (PerkinElmer). All the quantifications of ROS and JC1 were performed using Columbus Software.

### Cholesterol measurement

Relative intracellular cholesterol concentration was measured using Cholesterol Assay Kit, based on filipin fluorescent sensor<sup>47</sup> (Cell-Based) (Abcam, ab133116) according to manufacturer's recommendations. Quantification was performed using ImageJ Software.

### PMVK kinase assay

The assay is based on an enzymatic coupling system using the Pyruvate kinase (PK), Pyruvate Oxidase (PO) and the Horse Radish Peroxidase (HRP). The reaction synthesizing Diphosphomevalonate by the PMVK is measured through the ADP produced simultaneously, detected through its capacity to engage enzymatic coupling of PK, PO, and HRP through pyruvate and H<sub>2</sub>O<sub>2</sub> intermediates and the oxidation of Amplex red into the fluorescent compounds Resazurin. Six days after infection, MRC5 cells were washed twice with ice-cold KH buffer (50 mM HEPES, 110 mM KOAc, pH 7.2). Then cells were transferred on ice and incubated in KHM buffer (110 mM KOAc, 20 mM HEPES, 2 mM MgOAc, pH 7.2) containing 500 µg/ml of digitonin. After 5 min the supernatants were collected on ice and frozen at -20 °C. Lysates were thawed and then mixed v/v with a buffer containing HEPES pH 7.2 30 mM, NaCl 40 mM, EGTA 2 mM, Tween 20 0.04%, MgCl<sub>2</sub> 20 mM, BSA 0.2%. Thirty µL of this assay buffer was deposited in black fluorescent plate (2 replicates to test the kinase activity in presence or in absence of Phosphomevalonate (PMV) in the assay). Two buffers A and B were prepared in parallel, containing

respectively 50 mM KH<sub>2</sub>PO<sub>4</sub> pH 7, 375 µM Amplex Red (Sigma-Aldrich, Ampliflu™ Red, 90101) and KH<sub>2</sub>PO<sub>4</sub> 50 mM pH 7, MgCl<sub>2</sub> 2.5 mM, FAD 25 µM, Thiamine pyrophosphate 250 µM, Phosphoenol-pyruvate 2.5 mM (Megazyme), Horse Radish Peroxidase (5 U/mL) (Sigma-Aldrich, P8375), Pyruvate Kinase (15 U/mL) (from *Bacillus stearothermophilus*, Nipro), Pyruvate Oxidase (1.87 U/mL) (Sorachim-PYO-311). Also a solution of ATP (S1), or a mix of ATP and phospho-mevalonate (S2), was prepared in order to obtain 400 µM of each in the assay buffer by adding 5 µL of these solutions. At this step, 5 µL of S1 or S2 was first mixed with 40 µL of buffer B and then mixed again with 20 µL of buffer A. These mixtures containing either S1 or S2 were added to each tested sample and the plate was immediately incubated at 30 °C in fluorescent plate reader (Clariostar, BMG-Labtech). Real-time increase of fluorescence of resazurin produced from Amplex red oxidation was followed during 45 min. At the end of the experiment, slopes of the curves were analyzed to retain the linear increase of fluorescence, a time window where sufficient amount of ADP has accumulated to maintain a constant activity of the enzymatic coupling system. Slope obtained with only ATP in the reaction was subtracted from that corresponding to the same sample analyzed in presence of both ATP and PMV, and plotted as a curve of PMVK-dependent fluorescence increase by unit of time.

### Seahorse

Cells were plated in Seahorse seeding 24-well plates prior infection. Infection was performed in the 24-well plates and cells were subsequently selected for 5 days with Geneticin (ThermoFisher Scientific) at 75 µg/mL. Using Seahorse XF Cell Mito Stress Test (Agilent, Santa Clara) as described in<sup>44</sup>, fibroblasts were sequentially treated with 1.5 µM oligomycin, 1.5 µM phenylhydrazone (FCCP), and 0.5 µM Rotenone and Antimycin A. After assay, cells were stained with Hoescht for 10mn before proceeding to cell number counting and subsequent normalization. Data were obtained at SFR Biosciences AniRA-ImmO Platform, ENS de Lyon. Seahorse XFe Wave Software (Agilent) was used to subsequently analyze the data.

### Electron microscopy

1:1 volume of glutaraldehyde 4% was added to the culture medium and cells were incubated 15 min at 4 °C. After discarding medium/glutaraldehyde, 1:1 volume of glutaraldehyde 4% / cacodylate 0.2 M pH 7.4 was added. After fixation in glutaraldehyde 2%, cells were washed three times for 1 hr at 4 °C, post-fixed with 2% OsO<sub>4</sub> 1 hr at 4 °C, and dehydrated with an increasing ethanol gradient. Impregnation was performed with Epon A (50%) plus Epon B (50%) plus DMP30 (1.7%). Inclusion was obtained by polymerisation at 60 °C for 72 h. Ultrathin sections (approximately 70 nm thick) were cut on a UCT (Leica) ultramicrotome, mounted on 200 mesh copper grids and contrasted with uranyl acetate and lead citrate. Acquisition of at least 100 mitochondria of 10–20 independent cells per condition was performed with a Jeol 1400JEM (Tokyo, Japan) transmission electron microscope equipped with an Orius 600 camera and Digital Micrograph at CIQLE platform (UCBL-Lyon).

### Immunoblot and Immunofluorescence

For immunoblot experiments, cells were lysed in RIPA buffer. After protein quantification using Bradford assay, 30 µg of proteins were loaded and resolved by SDS-PAGE electrophoresis and transferred to nitrocellulose membranes (Bio-Rad). Membranes were blocked with TBS-Tween / Milk 5% for 1 h and incubated at 4 °C with primary antibodies overnight. Membranes were then incubated with secondary antibody for 1 h at room temperature. Detection was performed using ECL kit (Amersham). Each image of blots derive from the same experiment and all the samples of each experiment were processed in parallel. For immunofluorescence

experiments, cells were washed with PBS 1X, fixed for 15 min in 3.7% formaldehyde and permeabilized with Triton 100 × 0.1% for 10 min. Blocking was performed using PBS with 20% FBS during 30 min and cells were then incubated at 4 °C with primary antibodies overnight. Cells were incubated with secondary antibody for 1 h at room temperature, and washed before proceeding to image acquisition and analyses. Quantification was performed with ImageJ software. All primary antibodies and dilutions used are listed in Supplementary Table 2.

### Statistical analysis

Individual values represent mean ± SEM of n independent biological replicates for in vitro or n mice for in vivo, as mentioned in the figure legends. Shapiro-Wilk normality tests were applied to raw data before proceeding to any analyses. All further statistical analyses and tests are clearly indicated in figure legends. For groups not following normal distributions, nonparametric Mann-Whitney test was performed. For two groups both following normal distributions, parametric tests were two-tailed and performed as following Student's t-test (equal variance) or Welch's t-test (non-equal variance). For more than two groups, repeated measure (RM) (for paired data) or ordinary (for unpaired data) one-way ANOVA was used and Tukey's multiple comparisons test (with a single pooled variance) was subsequently performed. For in vivo data, two-sided Grubb's test was performed to find outliers, which were removed from further analysis if *p* value was below 0.05, and ordinary two-way ANOVA was used. All the statistical analyses were performed using GraphPad Prism Software 9.1.0 (*ns*: non-significant; \**p* < 0.05; \*\**p* < 0.01; \*\*\**p* < 0.001).

### Reporting summary

Further information on research design is available in the Nature Research Reporting Summary linked to this article.

### DATA AVAILABILITY

The data that support the findings of this study are available from the corresponding authors.

Received: 19 April 2023; Accepted: 30 October 2023;

Published online: 12 January 2024

### REFERENCES

- Gorgoulis, V. et al. Cellular Senescence: Defining a Path Forward. *Cell* **179**, 813–827 (2019).
- Muñoz-Espín, D. & Serrano, M. Cellular senescence: from physiology to pathology. *Nat. Rev. Mol. Cell Biol.* **15**, 482–496 (2014).
- He, S. & Sharpless, N. E. Senescence in Health and Disease. *Cell* **169**, 1000–1011 (2017).
- Herbig, U., Ferreira, M., Condel, L., Carey, D. & Sedivy, J. M. Cellular Senescence in Aging Primates. *Science* **311**, 1257–1257 (2006).
- Jeyapalan, J. C., Ferreira, M., Sedivy, J. M. & Herbig, U. Accumulation of Senescent Cells in Mitotic Tissue of Aging Primates. *Mech. Ageing Dev.* **128**, 36–44 (2007).
- Tuttle, C. S. L. et al. Cellular senescence and chronological age in various human tissues: A systematic review and meta-analysis. *Ageing Cell* **19**, e13083 (2020).
- Baker, D. J. et al. Clearance of p16lnk4a-positive senescent cells delays ageing-associated disorders. *Nature* **479**, 232–236 (2011).
- Baker, D. J. et al. Naturally occurring p16lnk4a-positive cells shorten healthy lifespan. *Nature* **530**, 184–189 (2016).
- van Deursen, J. M. Senolytic therapies for healthy longevity. *Science* **364**, 636–637 (2019).
- Zwerschke, W. et al. Metabolic analysis of senescent human fibroblasts reveals a role for AMP in cellular senescence. *Biochem. J.* **376**, 403–411 (2003).
- Dörr, J. R. et al. Synthetic lethal metabolic targeting of cellular senescence in cancer therapy. *Nature* **501**, 421–425 (2013).
- James, E. L. et al. Senescent human fibroblasts show increased glycolysis and redox homeostasis with extracellular metabolomes that overlap with those of

- irreparable DNA damage, aging, and disease. *J. Proteome Res.* **14**, 1854–1871 (2015).
- Ziegler, D. V., Wiley, C. D. & Velarde, M. C. Mitochondrial effectors of cellular senescence: beyond the free radical theory of aging. *Ageing Cell* **14**, 1–7 (2015).
- James, E. L., Lane, J. A. E., Michalek, R. D., Karoly, E. D. & Parkinson, E. K. Replicatively senescent human fibroblasts reveal a distinct intracellular metabolic profile with alterations in NAD<sup>+</sup> and nicotinamide metabolism. *Sci. Rep.* **6**, 38489 (2016).
- Flor, A. C., Wolfgeher, D., Wu, D. & Kron, S. J. A signature of enhanced lipid metabolism, lipid peroxidation and aldehyde stress in therapy-induced senescence. *Cell Death Discov* **3**, 17075 (2017).
- Johmura, Y. et al. Senolysis by glutaminolysis inhibition ameliorates various age-associated disorders. *Science* **371**, 265–270 (2021).
- Wiley, C. D. et al. Oxylipin biosynthesis reinforces cellular senescence and allows detection of senolysis. *Cell Metab* **33**, 1124–1136.e5 (2021).
- Gitenay, D. et al. Glucose metabolism and hexosamine pathway regulate oncogene-induced senescence. *Cell Death Dis* **5**, e1089 (2014).
- Wiley, C. D. et al. Mitochondrial Dysfunction Induces Senescence with a Distinct Secretory Phenotype. *Cell Metab* **23**, 303–314 (2016).
- Jones, R. G. et al. AMP-activated protein kinase induces a p53-dependent metabolic checkpoint. *Mol. Cell* **18**, 283–293 (2005).
- Wang, W., Yang, X., López de Silanes, I., Carling, D. & Gorospe, M. Increased AMP:ATP ratio and AMP-activated protein kinase activity during cellular senescence linked to reduced HuR function. *J. Biol. Chem.* **278**, 27016–27023 (2003).
- Nacarelli, T. et al. NAD<sup>+</sup> metabolism governs the proinflammatory senescence-associated secretome. *Nat. Cell Biol.* **21**, 397–407 (2019).
- Song, X. et al. Autophagy deficient keratinocytes display increased DNA damage, senescence and aberrant lipid composition after oxidative stress in vitro and in vivo. *Redox Biol.* **11**, 219–230 (2017).
- Venable, M. E., Lee, J. Y., Smyth, M. J., Bielawska, A. & Obeid, L. M. Role of Ceramide in Cellular Senescence. *J. Biol. Chem.* **270**, 30701–30708 (1995).
- Maeda, M., Scaglia, N. & Igal, R. A. Regulation of fatty acid synthesis and Δ<sup>9</sup>-desaturation in senescence of human fibroblasts. *Life Sci* **84**, 119–124 (2009).
- Inoue, C. et al. SMARCD1 regulates senescence-associated lipid accumulation in hepatocytes. *Npj Aging Mech. Dis* **3**, 1–9 (2017).
- Ogrodnik, M. et al. Cellular senescence drives age-dependent hepatic steatosis. *Nat. Commun.* **8**, 15691 (2017).
- Cadenas, C. et al. Glycerophospholipid profile in oncogene-induced senescence. *Biochim. Biophys. Acta* **1821**, 1256–1268 (2012).
- Lizardo, D. Y., Lin, Y.-L., Gokcumen, O. & Atilla-Gokcumen, G. E. Regulation of lipids is central to replicative senescence. *Mol. Biosyst.* **13**, 498–509 (2017).
- Millner, A. & Atilla-Gokcumen, G. E. Lipid Players of Cellular Senescence. *Metabolites* **10**, 339 (2020).
- Flor, A. C., Doshi, A. P. & Kron, S. J. Modulation of therapy-induced senescence by reactive lipid aldehydes. *Cell Death Discov* **2**, 1–10 (2016).
- Liu, X. et al. Reprogramming lipid metabolism prevents effector T cell senescence and enhances tumor immunotherapy. *Sci. Transl. Med.* **13**, (2021).
- Goldstein, J. L. & Brown, M. S. Regulation of the mevalonate pathway. *Nature* **343**, 425–430 (1990).
- Assmus, B. et al. HMG-CoA Reductase Inhibitors Reduce Senescence and Increase Proliferation of Endothelial Progenitor Cells via Regulation of Cell Cycle Regulatory Genes. *Circ. Res.* **92**, 1049–1055 (2003).
- Kim, R. H. et al. Bisphosphonates Induce Senescence in Normal Human Oral Keratinocytes. *J. Dent. Res.* **90**, 810–816 (2011).
- Ferrand, M. et al. Screening of a kinase library reveals novel pro-senescence kinases and their common NF-κB-dependent transcriptional program. *Ageing* **7**, 986–1003 (2015).
- Boehm, J. S. et al. Integrative genomic approaches identify IKBKE as a breast cancer oncogene. *Cell* **129**, 1065–1079 (2007).
- Herdendorf, T. J. & Mizioro, H. M. Phosphomevalonate Kinase: Functional Investigation of the Recombinant Human Enzyme. *Biochemistry* **45**, 3235–3242 (2006).
- Goldman, R. D. et al. Accumulation of mutant lamin A causes progressive changes in nuclear architecture in Hutchinson-Gilford progeria syndrome. *Proc. Natl. Acad. Sci. USA* **101**, 8963–8968 (2004).
- Mijit, M., Caracciolo, V., Melillo, A., Amicarelli, F. & Giordano, A. Role of p53 in the Regulation of Cellular Senescence. *Biomolecules* **10**, 420 (2020).
- Quinlan, C. L., Perevoshchikova, I. V., Hey-Mogensen, M., Orr, A. L. & Brand, M. D. Sites of reactive oxygen species generation by mitochondria oxidizing different substrates. *Redox Biol.* **1**, 304–312 (2013).
- Moiseeva, O., Bourdeau, V., Roux, A., Deschênes-Simard, X. & Ferbeyre, G. Mitochondrial dysfunction contributes to oncogene-induced senescence. *Mol. Cell Biol.* **29**, 4495–4507 (2009).
- Sivandzade, F., Bhalerao, A. & Cuccullo, L. Analysis of the Mitochondrial Membrane Potential Using the Cationic JC-1 Dye as a Sensitive Fluorescent Probe. *Bio-Protoc* **9**, e3128 (2019).

44. Gu, X., Ma, Y., Liu, Y. & Wan, Q. Measurement of mitochondrial respiration in adherent cells by Seahorse XF96 Cell Mito Stress Test. *STAR Protoc* **2**, 100245 (2021).
45. Annesley, S. J. & Fisher, P. R. Mitochondria in Health and Disease. *Cells* **8**, 680 (2019).
46. Fajtg, J., Davey, T., Turnbull, D. M., White, K. & Vincent, A. E. Mitochondrial morphology and function: two for the price of one! *J. Microsc.* **278**, 89–106 (2020).
47. Maxfield, F. R. & Wüstner, D. Analysis of cholesterol trafficking with fluorescent probes. *Methods Cell Biol.* **108**, 367–393 (2012).
48. Wang, B. & Tontonoz, P. Liver X receptors in lipid signalling and membrane homeostasis. *Nat. Rev. Endocrinol.* **14**, 452–463 (2018).
49. Audet-walsh, É. & Giguère, V. The multiple universes of estrogen-related receptor  $\alpha$  and  $\gamma$  in metabolic control and related diseases. *Acta Pharmacol. Sin.* **36**, 51–61 (2015).
50. Wei, W. et al. Ligand Activation of ERR $\alpha$  by Cholesterol Mediates Statin and Bisphosphonate Effects. *Cell Metab* **23**, 479–491 (2016).
51. Laganière, J. et al. A polymorphic autoregulatory hormone response element in the human estrogen-related receptor alpha (ERR $\alpha$ ) promoter dictates peroxisome proliferator-activated receptor gamma coactivator-1 $\alpha$  control of ERR $\alpha$  expression. *J. Biol. Chem.* **279**, 18504–18510 (2004).
52. Ogrodnik, M. & Jurk, D. Senescence explains age- and obesity-related liver steatosis. *Cell Stress* **1**, 70–72 (2017).
53. Modi, W. S. & Yoshimura, T. Isolation of novel GRO genes and a phylogenetic analysis of the CXC chemokine subfamily in mammals. *Mol. Biol. Evol.* **16**, 180–193 (1999).
54. B'chir, W. et al. Divergent Role of Estrogen-Related Receptor  $\alpha$  in Lipid- and Fasting-Induced Hepatic Steatosis in Mice. *Endocrinology* **159**, 2153–2164 (2018).
55. Smith, U., Li, Q., Rydén, M. & Spalding, K. L. Cellular senescence and its role in white adipose tissue. *Int. J. Obes.* **2005**, 45, 934–943 (2021).
56. Rezaie-Majd, A. et al. Simvastatin reduces expression of cytokines interleukin-6, interleukin-8, and monocyte chemoattractant protein-1 in circulating monocytes from hypercholesterolemic patients. *Arterioscler. Thromb. Vasc. Biol.* **22**, 1194–1199 (2002).
57. Sakoda, K. et al. Simvastatin Decreases IL-6 and IL-8 Production in Epithelial Cells: *J. Dent. Res.* <https://doi.org/10.1177/154405910608500608>. (2016).
58. Griveau, A. et al. Targeting the phospholipase A2 receptor ameliorates premature aging phenotypes. *Aging Cell* **17** (2018).
59. Wang, S.-T. et al. Atorvastatin-induced senescence of hepatocellular carcinoma is mediated by downregulation of hTERT through the suppression of the IL-6/STAT3 pathway. *Cell Death Discov* **6**, 17 (2020).
60. Liu, S. et al. *assmu*. *Sci. Rep.* **5**, 1–11 (2015).
61. Montecucco, F. & Mach, F. Update on statin-mediated anti-inflammatory activities in atherosclerosis. *Semin. Immunopathol.* **31**, 127–142 (2009).
62. Liou, C.-J. et al. Oral Lovastatin Attenuates Airway Inflammation and Mucus Secretion in Ovalbumin-Induced Murine Model of Asthma. *Allergy Asthma Immunol. Res.* **6**, 548–557 (2014).
63. Liao, J. K. & Laufs, U. Pleiotropic effects of statins. *Annu. Rev. Pharmacol. Toxicol.* **45**, 89–118 (2004).
64. Roelofs, A. J., Thompson, K., Gordon, S. & Rogers, M. J. Molecular Mechanisms of Action of Bisphosphonates: Current Status. *Clin. Cancer Res.* **12**, 6222s–6230s (2006).
65. Baziotti, V. et al. T cell cholesterol efflux suppresses apoptosis and senescence and increases atherosclerosis in middle aged mice. *Nat. Commun.* **13**, 3799 (2022).
66. Roh, K. et al. Lysosomal control of senescence and inflammation through cholesterol partitioning. *Nat. Metab.* **5**, 398–413 (2023).
67. Clarke, P. R. & Hardie, D. G. Regulation of HMG-CoA reductase: identification of the site phosphorylated by the AMP-activated protein kinase in vitro and in intact rat liver. *EMBO J* **9**, 2439–2446 (1990).
68. Sapir, A. et al. Controlled sumoylation of the mevalonate pathway enzyme HMGS-1 regulates metabolism during aging. *Proc. Natl. Acad. Sci. USA* **111**, E3880–E3889 (2014).
69. Luo, J., Yang, H. & Song, B.-L. Mechanisms and regulation of cholesterol homeostasis. *Nat. Rev. Mol. Cell Biol.* **21**, 225–245 (2020).
70. d'Adda di Fagagna, F. Living on a break: cellular senescence as a DNA-damage response. *Nat. Rev. Cancer* **8**, 512–522 (2008).
71. Miwa, S. et al. Low abundance of the matrix arm of complex I in mitochondria predicts longevity in mice. *Nat. Commun.* **5**, 3837 (2014).
72. Zdanov, S. et al. Normal or stress-induced fibroblast senescence involves COX-2 activity. *Exp. Cell Res.* **313**, 3046–3056 (2007).
73. Pantazi, A. et al. Inhibition of the 60S ribosome biogenesis GTPase LSG1 causes endoplasmic reticular disruption and cellular senescence. *Aging Cell* **18**, e12981 (2019).
74. Hamsanathan, S. & Gurkar, A. U. Lipids as Regulators of Cellular Senescence. *Front. Physiol.* **13**, 796850 (2022).
75. Augert, A. et al. The M-type receptor PLA2R regulates senescence through the p53 pathway. *EMBO Rep.* **10**, 271–277 (2009).
76. Vindrieux, D. et al. PLA2R1 mediates tumor suppression by activating JAK2. *Cancer Res.* **73**, 6334–6345 (2013).
77. Griveau, A., Wiel, C., Ziegler, D. V., Bergo, M. O. & Bernard, D. The JAK1/2 inhibitor ruxolitinib delays premature aging phenotypes. *Aging Cell* **19**, e13122 (2020).
78. Griveau, A. et al. The PLA2R1-JAK2 pathway upregulates ERR $\alpha$  and its mitochondrial program to exert tumor-suppressive action. *Oncogene* **35**, 5033–5042 (2016).
79. Teyssier, C. et al. Absence of ERR $\alpha$  in female mice confers resistance to bone loss induced by age or estrogen-deficiency. *PLoS One* **4**, e7942 (2009).
80. Delhon, I. et al. Absence of estrogen receptor-related-alpha increases osteoblastic differentiation and cancellous bone mineral density. *Endocrinology* **150**, 4463–4472 (2009).
81. Farr, J. N. et al. Targeting cellular senescence prevents age-related bone loss in mice. *Nat. Med.* **23**, 1072–1079 (2017).
82. Kanis, J. A. et al. European guidance for the diagnosis and management of osteoporosis in postmenopausal women. *Osteoporos. Int.* **19**, 399–428 (2008).
83. Scaffidi, P. & Misteli, T. Lamin A-dependent misregulation of adult stem cells associated with accelerated ageing. *Nat. Cell Biol.* **10**, 452–459 (2008).
84. Debacq-Chainiaux, F., Erusalimsky, J. D., Campisi, J. & Toussaint, O. Protocols to detect senescence-associated beta-galactosidase (SA- $\beta$ gal) activity, a biomarker of senescent cells in culture and in vivo. *Nat. Protoc.* **4**, 1798–1806 (2009).

## ACKNOWLEDGEMENTS

We thank laboratory members for helpful suggestions and collaborations. This work was supported by the Ligue Régionale contre le Cancer (Comité du Rhône) (NM) and ANR (ANR-14-CE12-0003) (DB). Institut Convergence PLACAN, ANR-17-CONV-0002 also support the project. DZ was supported by the French Ministry of Higher Education and Research and by the Fondation pour la Recherche Médicale FRM (FDT201904008259).

## AUTHOR CONTRIBUTIONS

D.V.Z., J.C.H., M.V., A.H., A.M., C.M., A.G., A.V. and C.C. performed in vitro experiments. M.V., C.S. and J.R. performed in vivo experiments. D.V.Z., M.V., V.G., A.V., J.G., N.M. and D.B. designed the experiments and the results were analyzed by all the co-authors. D.V.Z., N.M. and D.B. designed the overall study. D.B. and N.M. co-supervised the work. D.V.Z., N.M. and D.B. wrote the manuscript with input from all authors.

## COMPETING INTERESTS

The authors declare no competing interests.

## ADDITIONAL INFORMATION

**Supplementary information** The online version contains supplementary material available at <https://doi.org/10.1038/s41514-023-00128-y>.

**Correspondence** and requests for materials should be addressed to Nadine Martin or David Bernard.

**Reprints and permission information** is available at <http://www.nature.com/reprints>

**Publisher's note** Springer Nature remains neutral with regard to jurisdictional claims in published maps and institutional affiliations.



**Open Access** This article is licensed under a Creative Commons

Attribution 4.0 International License, which permits use, sharing, adaptation, distribution and reproduction in any medium or format, as long as you give appropriate credit to the original author(s) and the source, provide a link to the Creative Commons license, and indicate if changes were made. The images or other third party material in this article are included in the article's Creative Commons license, unless indicated otherwise in a credit line to the material. If material is not included in the article's Creative Commons license and your intended use is not permitted by statutory regulation or exceeds the permitted use, you will need to obtain permission directly from the copyright holder. To view a copy of this license, visit <http://creativecommons.org/licenses/by/4.0/>.

© The Author(s) 2024